e-Science Journal
Global Scientific Information and Computing Center
Vol. 9

TSUBAME ESJ.

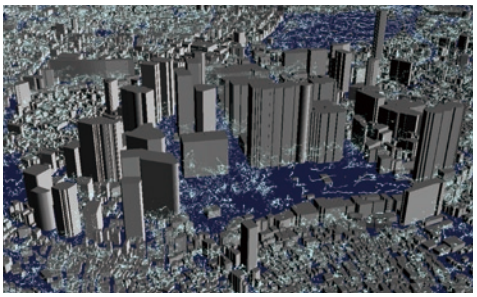

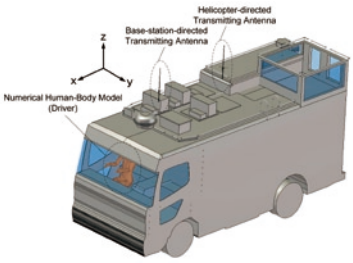

Large-scale LES Wind Simulation using Lattice Boltzmann Method for a 10km x 10km Area in Metropolitan Tokyo

Evaluation of Electromagnetic Wave Exposure by Large-scale Electromagnetic Field Analysis in Response to the Frequency Migration of Mobile-relay FPUs

All-Atom Simulation of a Cell Membrane System of Photosynthetic Bacteria Using Large-Scale GPU Calculation

Large-scale LES Wind Simulation using Lattice Boltzmann Method for a 10 km x 10 km Area in Metropolitan Tokyo

Naoyuki Onodera* Takayuki Aoki* Takashi Shimokawabe* Hiromichi Kobayashi**

* Tokyo Institute of Technology, Global Scientific Information and Computing Center

** Keio University, Research and Education Center for Natural Sciences

A lot of tall buildings and complex structures make the air flow turbulent in large urban areas. In order to understand the details of airflows in such areas, it is necessary to carry out large-scale Computational Fluid Dynamics (CFD) simulations. We developed a CFD code based on the Lattice Boltzmann Method (LBM). Since airflows in large cities are turbulent with Reynolds numbers of several million, a Large-Eddy Simulation (LES) model has to be used to solve the LBM equation. The dynamic Smagorinsky model is often used, but it requires an average to be taken over a wide area to determine the model constant. Since there is a huge overhead for large-scale computations, we applied the coherent-structure Smagorinsky model that does not use any spatial averages and is able to determine the model constant locally. We generated the computational boundary condition based on real building data and carried out a domain decomposition for multiple-GPU computing on TSUBAME 2.0. The code is written in CUDA, and the GPU kernel function is well tuned to achieve high performance on Fermi-core GPUs. By introducing an overlapping technique between GPU-to-GPU communication and GPU kernel computation, we improved the computational efficiency of large-scale computations by 30 % . Although the LBM computation is essentially memory bound, we obtained fairly good performances for both strong and weak scalabilities. We used 4,032 GPUs for a computation with a 10,080 × 10,240 × 512 mesh. By executing this large-scale computation, details of the wind behind buildings, the "wind street" along a big streets, typhoon damage, etc., were revealed with much higher accuracy than ever before. An unprecedentedly detailed LES computation with a 1-m resolution was conducted on a 10 km × 10 km urban area of Tokyo.

1 Introduction

Pedestrians often feel strong winds around tall buildings in the metropolitan Tokyo area. The concentration of tall buildings makes the air flow turbulent. In order to understand the details of the airflow there, it is necessary to carry out large-scale Computational Fluid Dynamics (CFD) simulations, but thanks to recent progress in supercomputers, we can now execute large-scale computation using a billion mesh points. Air flows behave as almost incompressible fluids in a wide area of metropolitan Tokyo. In order to have much larger time steps than those restricted by the sound velocity, semi-Lagrangian methods are often used to perform a time integration in which the pressure Poisson equation is iteratively solved with a sparse matrix solver. In such large-scale problems, it is rather difficult for sparse matrix solvers to converge efficiently because of pre-conditioners and the overhead of node-to-node intercommunication.

The Lattice Boltzmann Method (LBM) is a class of CFD methods that solve the discrete-velocity Boltzmann equation. In this method, the time integration is explicit, and the Poisson equation is not solved. In addition, LBM continuously accesses memory with a simple algorithm and is suitable for large-scale computations including complicated objects. As an example, researches performing large-scale calculation using LBM [1] won the Gordon Bell prize in SC10. Moreover, fluid phenomena taking into consideration complex shapes have also been studied [2][3]. However, LBM has not been applied to turbulent flows at high Reynolds numbers. So far, there has been no large-scale wind flow simulation accounting for real building shapes. A Large-Eddy Simulation (LES) is an approach that can deal with unsteady turbulent flows. It is expected that the application of LES to LBM would allow one to make a stable calculation of turbulent flows with high Reynolds number [4]. The dynamic Smagorinsky model [5][6] is a prominent subgrid-scale model based on the concept of eddy viscosity. However, to determine the model parameter, a spatial average has to be carried out over the global domain. This makes the computation too inefficient for large-scale simulations. The coherent-structure model (CSM) [7] is a remedy to these problems; it enables the model parameter to be locally calculated without taking any averages. CSM is suitable for a large-scale LBM computation, and in this study, we applied it to a LES wind simulation.

Lattice Boltzmann method 2

LBM solves the discrete Boltzmann equation to simulate the flow of a Newtonian fluid. The flow field is expressed by a limited number of pseudo particles in a streaming and collision process. The physical space is discretized by a uniform grid. Since pseudo particles move onto the neighbor lattice points after one time step in the streaming process, this process is completed without any error. The macroscopic diffusion and the pressure gradient are expressed by the collisional process, and we used the BGK model[8], as most of the previous studies did. The time evolution of the discretized velocity function is

$$f_i(x + c_i\Delta t, t + \Delta t) = f_i(x,t) - \frac{1}{\tau}(f_i(x,t) - f_i^{eq}(x,t)) + F_i(x,t). \quad (1)$$

Here, Δt is the time interval, τ the relaxation time, and $f_i^{eq}(x,t)$ the local equilibrium distribution at time t and position x. In the D3Q19 model, the components of the velocity vector are

$$c_i = \begin{cases} (0,0,0) & i = 0, \\ (\pm c,0,0),(0,\pm c,0),(0,0,\pm c) & i = \text{1-6}, \\ (\pm c,\pm c,0),(\pm c,0,\pm c),(0,\pm c,\pm c) & i = \text{7-18}. \end{cases} \quad (2)$$

We used the following local equilibrium distribution

$$f_i^{eq} = w_i\rho\left(1 + \frac{3c_i \cdot u}{c^2} + \frac{9(c_i \cdot u)^2}{2c^4} - \frac{3u^2}{2c^2}\right) \quad (3)$$

where ρ is the density and u is the macroscopic velocity. The corresponding weighting factors of the D3Q19 model are

$$w_i = \begin{cases} 1/3 & i = 0, \\ 1/18 & i = \text{1-6}, \\ 1/36 & i = \text{7-18}. \end{cases} \quad (4)$$

The relaxation time in the collisional process is determined using the dynamic viscosity,

$$\tau = \frac{1}{2} + \frac{3\nu}{c^2\Delta t}. \quad (5)$$

LBM is especially suitable for modeling boundary conditions with complex shapes. The bounce-back (BB) scheme and the interpolated bounce-back schemes [9][10] make it easy to implement the no-slip velocity condition. Immersed boundary methods (IBM) are able to handle complex boundary conditions by adding external forces [11] in LBM. Since the BB scheme directly applies these conditions to the distribution function, it should be able to obtain high enough efficiency for GPU computing. In this research, we applied the BB scheme to LBM.

Large-eddy simulation 3

A large-eddy simulation (LES) resolves the flow dynamics of large-scale structures on a grid scale (GS), and it takes into account the effect of smaller-scale turbulent structures by using a subgrid-scale (SGS) model. SGS models, which are based on the concept of eddy viscosity, evaluate the effect of turbulence as

$$\nu_{SGS} = C\bar{\Delta}^2\left|\bar{S}\right| \quad (6)$$

where C is the model coefficient, and $\bar{\Delta}$ is the filter width. The velocity strain tensor and its magnitude are defined as

$$\bar{S}_{ij} = \frac{1}{2}\left(\frac{\partial u_j}{\partial x_i} + \frac{\partial u_i}{\partial x_j}\right), \quad \left|\bar{S}\right| = \sqrt{2\bar{S}_{ij}\,\bar{S}_{ij}}. \quad (7)$$

3-1 Dynamic Smagorinsky model

In the conventional Smagorinsky model (SM), the model coefficient C is a constant in the entire computational domain, and the SGS viscosity does not describe the correct asymptotic behavior near a wall. The dynamic Smagorinsky model (DSM)[5][6] overcomes this defect by dynamically calculating the model parameter by using two types of grid filter. Although DSM is the most notable breakthrough in LES, the model parameter of DSM requires the average to be taken in the global domain for the sake of numerical stability. This introduces a large overhead fo large-scale simulations and makes it difficult to treat complex geometries.

3-2 Coherent-structure Smagorinsky model

The coherent structure model (CSM) [12] is a promising approach to solve the above problems. In CSM, we can determine the model parameters locally by using the information about the turbulent structure[7]. The model coefficient C_{CSM} is calculated by treating the coherent structure F_{CS} as a function of the second invariant of the velocity gradient tensor Q and the magnitude of the velocity gradient tensor E:

$$C_{CSM} = C' |F_{CS}|^{3/2},$$
$$F_{CS} = \frac{Q}{E} \quad (-1 \le F_{CS} \le 1), \tag{8}$$
$$Q = -\frac{1}{2}\frac{\partial \bar{u}_j}{\partial x_i}\frac{\partial \bar{u}_i}{\partial x_j}, \quad E = \frac{1}{2}\left(\frac{\partial \bar{u}_j}{\partial x_i}\right)^2.$$

The coefficient C' = 1/20 is a fixed model parameter, and it is optimized for a wide range of simulations. CSM is suitable for parallel computing without any average process.

3-3 Subgrid-scale eddy viscosity of the lattice Boltzmann method

Incorporation of CSM into LBM makes it possible to carry out a large-scale simulation with complex boundaries at high Reynolds numbers. The total relaxation time with the eddy viscosity is

$$\tau_* = \frac{1}{2} + \frac{3\nu_*}{c^2 \Delta t}, \qquad \nu_* = \nu_0 + \nu_t. \tag{9}$$

Optimization of the LBM computation for multiple GPU computing 4

The overlapping method is a technique to hide the communication time with the computation time [13][14]. A computational domain is divided into a central region and a boundary region. First, the GPU kernel for the boundary region launches and the GPU kernel for the central region and the GPU-to-GPU communication are executed simultaneously. The data communication between a host memory and a GPU device memory is performed done by using the CUDA runtime API "cudaMemcpyAsync", and we used the asynchronous MPI library for data communications between compute nodes.

Regarding the domain decomposition, we divide the domain two-dimensionally in the y- and z-directions. The components of the velocity distribution function with the velocity direction require communications about their directions. In particular, six components of the velocity distribution function $f_i = (0, \pm c, 0)$, $(\pm c, \pm c, 0)$ require MPI communications in the y-direction, six components $f_i = (0, 0, \pm c)$, $(\pm c, 0, \pm c)$ require MPI communications in the z-direction, and seven components $f_i = (0, \pm c, \pm c)$ and u_i require MPI communications in the y- and z-directions.

Performance on TSUBAME 2.0 5

The TSUBAME 2.0 supercomputer at the Tokyo Institute of Technology is equipped with more than 4,000 GPUs (NVIDIA TESLA M2050) and has achieved 1.192 PFLOPS on the Linpack benchmark. We measured the performance of our LBM code on TSUBAME 2.0.

5-1 Performance on a single GPU

In our GPU implementation, the streaming and collision processes are fused so as to reduce memory accesses. The GPU code is compiled with the support of the Super Function Unit (SFU) and a 32-bit mode in association with other optimized techniques. Figure 1 shows the performance of our LBM code to compare with the theoretical performance estimated by the improved roofline model, which is expressed in terms of the amount of arithmetic operations (F), the amount of data access (B), the peak performance (F_{peak}), and the peak memory bandwidth (B_{peak}):

$$P = \frac{F/B}{F/B + F_{peak}/B_{peak}} F_{peak}. \tag{10}$$

The following parameters were used in this estimation:

$$(F_{peak}, B_{peak}) = (1030GFLOPS,\ 148Gbyte/sec),$$
$$(F, B) = (476FLOPS,\ 260Byte),$$
$$(P, F/B) = (214GFLOPS,\ 1.83).$$

We achieved 198 GFLOPS in 32-bit mode in single precision. We have an 8 % performance increase with the 32-bit compile option. The performance efficiency relative to that of the

roofline model is 92% , and this means that the GPU kernel code is well-tuned on Fermi-core GPUs.

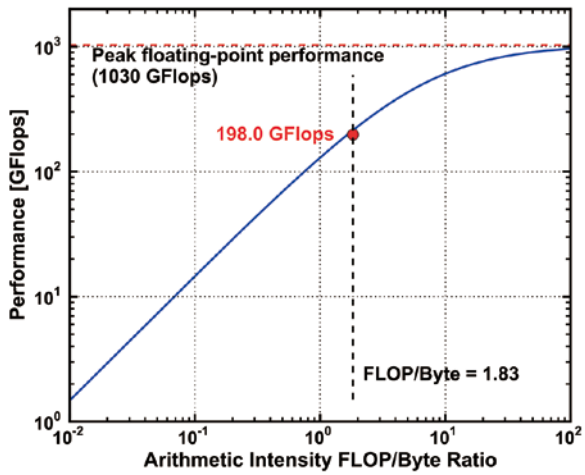

Fig. 1 Performance on single GPU (red point) and improved roofline model expressed by Eq.(10) (blue line).

5-2 Performance on multiple GPUs

Figures 2 and 3 present the weak and the strong scalabilities of the LBM performance on TSUBAME 2.0. In these figures, the horizontal axis indicates the number of GPUs, and the vertical axis the performance (TFLOPS) in single precision.

Regarding the weak scalability results, each GPU handled a domain with a 192 × 256 × 256 mesh. The overlapping technique improved scalability by 30% compared with the situation without overlapping. We achieved 115 TFLOPS using 768 GPUs and 149 TFLOPS using 1,000 GPUs, which is 15% of the peak performance.

Regarding the strong scalability, the overlapping technique hid communication costs more efficiently from 32 GPUs to 256 GPUs; the result on 64 GPUs was 97 % efficiency, the result on 128 GPUs was 87 % efficiency, and the result on 256 GPUs was 63% efficiency compared with the performance on 32 GPUs. Since the model parameter of CSM could be locally determined without averaging, we obtained fairly good performance for both strong and weak scalabilities.

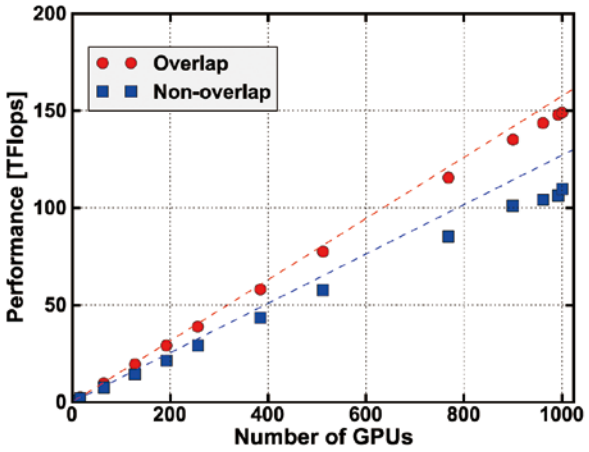

Fig. 2 Weak scalability in single precision.

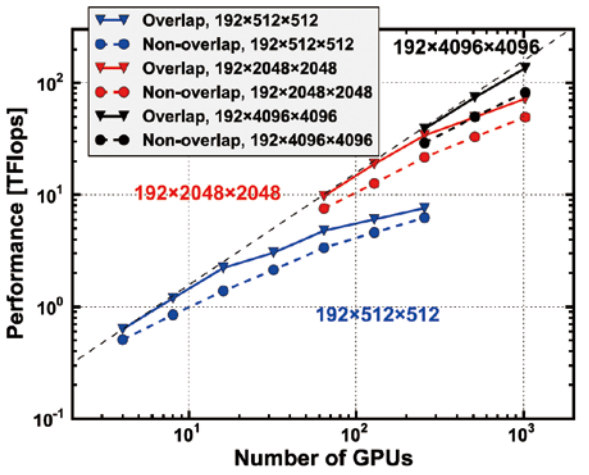

Fig. 3 Strong scalability in single precision.

Wind simulation in metropolitan Tokyo 6

The large-scale wind simulation of a 10 km × 10 km area had a resolution of 1 m and it included real building data of the city of Tokyo. The computational domain covered the major wards of Tokyo, including Shinjuku, Chiyoda, Chuo, Minato, and Meguro. We used 4,032 GPUs and a 10,080 × 10,240 × 512 mesh. The inflow and outflow conditions were applied in the streamwise direction (from north to south). Periodic boundary conditions were assumed in the spanwise direction (east and west). The ground had a non-slip condition. The inlet velocity was set to be $U_{in}=A \log_{10} z/z_0$, where the ground roughness was

z_0=2 and wind velocity was 10 m/s at a height of 100 m. The Reynolds number, which was evaluated from the inlet velocity, physical properties of the air, and heights of the buildings, was about 10^6. Since the Reynolds number was very high, the wind simulation without the SGS model was unstable and eventually numerically diverged.

Figure 4 shows the map of the Tokyo area in the computation (2012 Google ZENRIN), and Fig. 5 shows a snapshot of the wind flows visualized by using mass-less particles. It is clear that tall buildings affect the wind over a broad area, and a strong turbulent wind arises near Shinagawa Station.

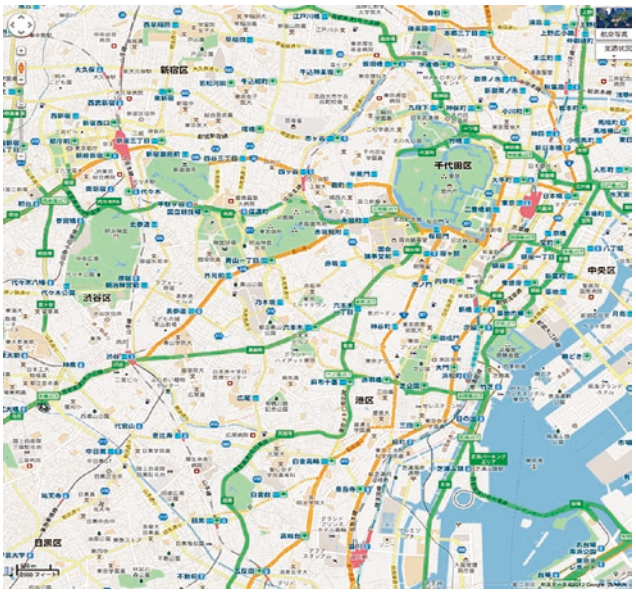

Fig. 4 Tokyo area corresponding to the computation (north is up).

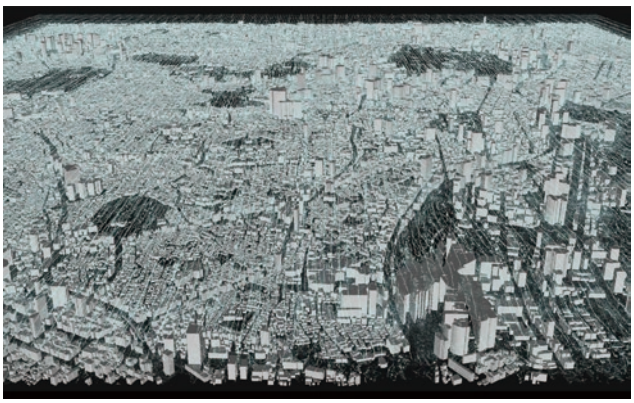

Fig. 5 Snapshot of wind flow using particles (north is up).

In order to study the wind flow in detail, we examined the instantaneous velocity profiles. Figure 6 shows a map of the Shinjuku area, and Fig. 7 shows the velocity profile at a height of 25 m. The blue area indicates the buildings. It is clear that strong winds blow along big streets and very complicated velocity profiles are generated behind tall buildings. Figure 8 shows the velocity profile at a height of 100 m. We can see that strong winds blow at higher altitudes and cause turbulence on the ground.

Figure 9 shows the vertical velocity profile along the red dotted line in Fig. 6. This figure shows that tall buildings push down high-velocity flows, and turbulent vortices behind buildings mix the atmosphere in the vertical direction. Figure 10 shows a snapshot of the wind flow using massless particles. The particles were generated at fixed points with time sequence. The figure shows that streamlines formed by the particles are strongly disturbed by the complicated flows behind the buildings, whereas the streamlines near low-rise buildings are not so disturbed.

The above results clearly show that by executing a large-scale LES wind simulation using detailed data on real buildings, we succeeded in getting a high-resolution profile of the airflows in metropolitan Tokyo.

Fig. 6 Shinjuku area (north is up).

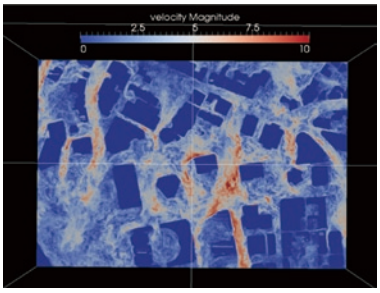

Fig. 7 Horizontal velocity profile (m/s) at a height of 25 m in the Shinjuku area (north is up).

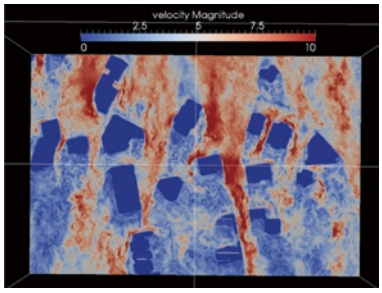

Fig. 8 Horizontal velocity profile (m/s) at a height of 100 m in the Shinjuku area (north is up).

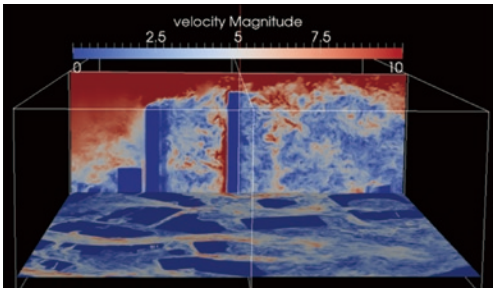

Fig. 9 Vertical velocity profile (m/s) in the Shinjuku area (north is left).

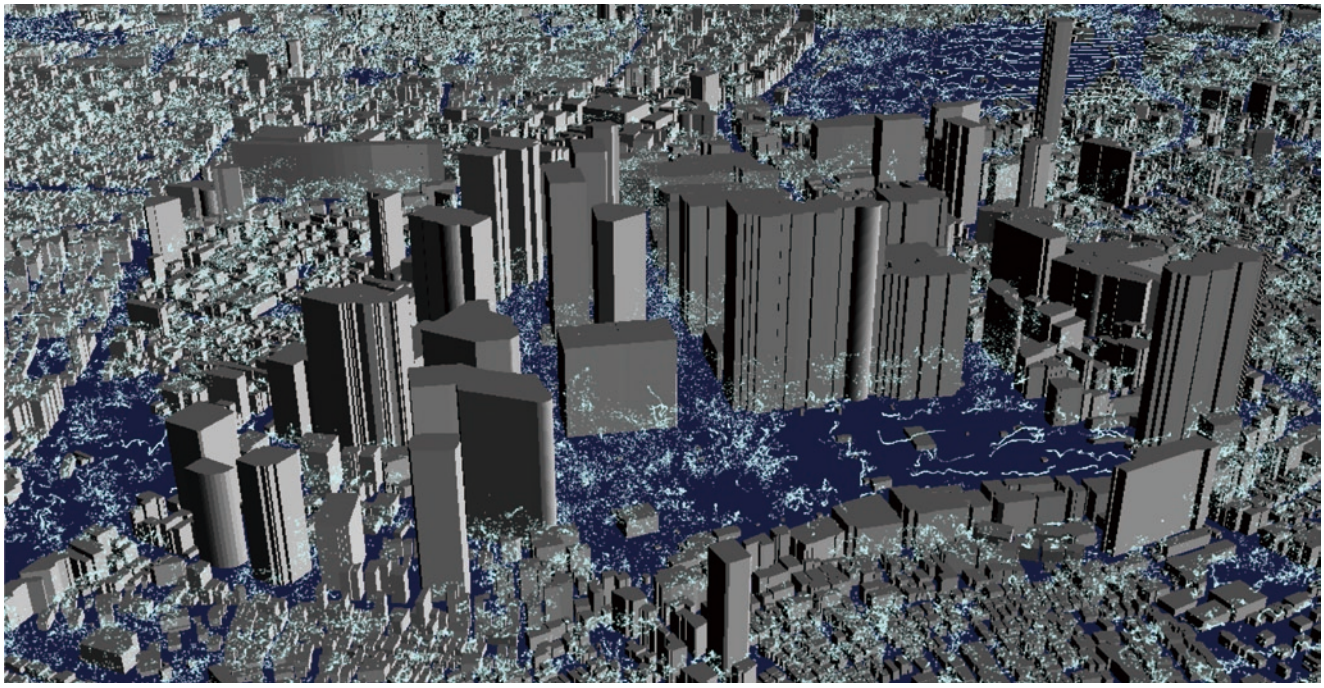

Fig. 10 Snapshot of wind flow using particles in the Shinjuku area (north is left).

Summary and conclusions 7

We presented a large-scale wind simulation accounting for data on real buildings in metropolitan Tokyo. The lattice Boltzmann method with the coherent-structure Smagorinsky model was applied to turbulent flows with Reynolds number of several million. The code was written in the GPU programming framework CUDA, and the GPU kernel functions were well tuned, achieving 92 % effective performance compared with the roofline model on a single GPU. We achieved 149 TFLOPS in single precision on 1,000 GPUs, which is 15 % of the peak performance, by using an overlapping technique.

The large-scale wind simulation covered a 10 km × 10 km area of downtown Tokyo to a resolution of 1 m, and the results revealed the large-scale structure of the wind, as well as detailed winds behind buildings, and the "wind street" along big streets.

We concluded that the present scheme is one of most promising approaches to simulating a wide area of turbulence. The LES computation for the 10 km × 10 km area with a 1-m resolution is the most extensive of its kind.

Acknowledgements

The above peta-scale simulations were executed as the TSUBAME Grand Challenge Program, Category A in 2012 fall and we would like express our special thanks to having a chance to use the whole TSUBAME resources and all the GSIC staffs who supported our project. This research was supported in part by the Japan Society for the Promotion of Science (KAKENHI), a Grant-in-Aid for Scientific Research (B) 23360046 from the Ministry of Education, Culture, Sports, Science and Technology (MEXT) of Japan, and Japan Science and Technology Agency (JST) Core Research of Evolutional Science and Technology (CREST) research programs on "ULP-HPC: Ultra Low-Power, High-Performance Computing via Modeling and Optimization of Next Generation HPC Technologies" and "Highly Productive, and High Performance Application Frameworks for Post Petascale Computing".

References

[1] A. Rahimian, I. Lashuk, S. Veerapaneni, A. Chandramowlishwaran, D. Malhotra, L. Moon, R. Sampath, A. Shringarpure, J. Vetter, R. Vuduc, et al. Petascale direct numerical simulation of blood flow on 200k cores and heterogeneous architectures. In Proceedings of the 2010 ACM/IEEE International Conference for High Performance Computing, Networking, Storage and Analysis, pages 1–11. IEEE Computer Society, 2010.

[2] X. Wang and T. Aoki. Multi-gpu performance of incompressible flow computation by lattice boltzmann method on gpu cluster. Parallel Computing, 2011.

[3] M. Bernaschi, M. Fatica, S. Melchionna, S. Succi, and E. Kaxiras. A flexible high-performance lattice boltzmann gpu code for the simulations of fluid flows in complex geometries. Concurrency and Computation: Practice and Experience, 22(1):1–14, 2009.

[4] H. Yu, S.S. Girimaji, and L.S. Luo. Dns and les of decaying isotropic turbulence with and without frame rotation using lattice boltzmann method. Journal of Computational Physics, 209(2):599–616, 2005.

[5] M. Germano, U. Piomelli, P. Moin, and W.H. Cabot. A dynamic subgrid-scale eddy viscosity model. Physics of Fluids A: Fluid Dynamics, 3:1760, 1991.

[6] DK Lilly. A proposed modification of the germano subgrid-scale closure method. Physics of Fluids A: Fluid Dynamics, 4:633, 1992.

[7] H.Kobayashi, F. Ham, and X. Wu. Application of a local sgs model based on coherent structures to complex geometries. International Journal of Heat and Fluid Flow, 29(3), 2008.

[8] Q. Zou and X. He. On pressure and velocity flow boundary conditions and bounceback for the lattice boltzmann bgk model. Arxiv preprint comp-gas/9611001, 1996.

[9] X. Yin and J. Zhang. An improved bounce-back scheme for complex boundary conditions in lattice boltzmann method. Journal of Computational Physics, 2012.

[10] B. Chun and AJC Ladd. Interpolated boundary condition for lattice boltzmann simulations of flows in narrow gaps. Physical review E, 75(6):066705, 2007.

[11] C. Shu, N. Liu, and YT Chew. A novel immersed boundary velocity correction–lattice boltzmann method and its application to simulate flow past a circular cylinder. Journal of Computational Physics, 226(2):1607–1622, 2007.

[12] H. Kobayashi. Large eddy simulation of magneto hydrodynamic turbulent channel flows with local subgrid-scale model based on coherent structures. Physics of Fluids, 18:045107, 2006.

[13] T. Shimokawabe, T. Aoki, C. Muroi, J. Ishida, K. Kawano, T. Endo, A. Nukada, N. Maruyama, and S. Matsuoka. An 80-fold speedup, 15.0 tflops full gpu acceleration of non-hydrostatic weather model asuca production code. In High Performance Computing, Networking, Storage and Analysis (SC), 2010 International Conference for, pages 1–11. IEEE, 2010.

[14] T. Shimokawabe, T. Aoki, T. Takaki, T. Endo, A. Yamanaka, N. Maruyama, A. Nukada, and S. Matsuoka. Peta-scale phase-field simulation for dendritic solidification on the tsubame 2.0 supercomputer. In Proceedings of 2011 International Conference for High Performance Computing, Networking, Storage and Analysis, page 3. ACM, 2011.

Evaluation of Electromagnetic Wave Exposure by Large-scale Electromagnetic Field Analysis in Response to the Frequency Migration of Mobile-relay FPUs

Naoto Kogo* Tetsuomi Ikeda**

* NHK Engineering Administration Department ** NHK Science & Technology Research Laboratories

NHK's field pickup unit (FPU) operating in the 700-MHz band is used for transmitting video and audio signals during mobile relays of marathons, long-distance relay races, and other road events, but Japan's Ministry of Internal Affairs and Communications (MIC) is now studying a migration to the 1.2-GHz and 2.3-GHz bands as part of a frequency-reorganization action plan. Since the target frequencies are higher than those in the 700-MHz band, propagation loss is greater, and we are now investigating the increasing of transmission power to compensate for that loss. Increasing transmission power, however, raises concerns about the effects of electromagnetic wave exposure on the announcer, driver, or other broadcast-van personnel in the vicinity of any transmitting antennas. For this reason, we analyzed the specific absorption rate (SAR) on human bodies by modeling transmitting antennas for FPU operation in the 700-MHz, 1.2-GHz, and 2.3-GHz bands and by analyzing the electromagnetic fields impacting the announcer and driver using a numerical human-body model.

1 Introduction

NHK currently uses a field pickup unit (FPU) [1] operating in the 700-MHz band (770 – 806 MHz) to transmit video and audio in mobile relays of marathons, long-distance relay races, and other road events. However, Japan's Ministry of Internal Affairs and Communications (MIC) is studying a migration of the FPU frequency band to the 1.2-GHz (1.24–1.3 GHz) and 2.3-GHz (2.33–2.37 GHz) bands as part of a frequency-reorganization action plan [2]. In these candidate frequency bands, however, free-space transmission loss and diffraction loss are high compared with that in the 700-MHz band, so we are studying ways of compensating for that loss such as by introducing a space-time trellis coded, multiple-input and multiple output (STTC-MIMO) scheme [3] or increasing the transmission power beyond that of the current FPU. Increasing the transmission power, however, raises concerns about the amount of electromagnetic power impacting broadcast-van personnel in the vicinity of any transmitting antennas compared with that of the current FPU.

When discussing the effects of electromagnetic wave exposure on the human body, it must be kept in mind that the applicable range of a "general environment" in radio-radiation protection guidelines [4] has been expanding as the usage scenarios of radio equipment become increasingly diversified. For example, studies have been performed on applying the acceptable specific absorption rate (SAR) not only to radio equipment used in close proximity to the side of the head as in mobile phone terminals but also to radio equipment that is normally used in such a way that the distance between the human body and the antenna is no more than 20 cm [5]. Specifically, radio-radiation protection guidelines have come to stipulate that, in a general environment, the 10g average local SAR [6] obtained by averaging SAR across any 10 grams of human-body tissue must not exceed 2 [W/kg] while the whole-body average SAR must not exceed 0.08 [W/kg].

On the other hand, the applicable range of a "managed environment" in radio-radiation protection guidelines is typically considered for special radio equipment such as that used in broadcasting [7, 8]. In this case, the guidelines stipulate that the 10g average local SAR must not exceed 10 [W/kg] while the whole-body average SAR must not exceed 0.4 [W/kg]. These guideline values are both five times that of a general environment. In FPU operation, though, an announcer, driver, and other personnel ride the broadcast van in close proximity to transmitting antennas, so it is necessary to perform evaluations in terms of a general environment. However, there are no examples of studies performed on electromagnetic wave exposure in an actual FPU-operating environment taking frequency migration into account.

In addition, taking measurements when evaluating electromagnetic wave exposure in the operation of a mobile-relay FPU can be difficult since information on the environment surrounding the human body such as the shape of the broadcast van must be included. Consequently, while evaluation by electromagnetic field analysis is an effective method, the large structure of the broadcast van as well as shorter wavelengths as a result of FPU frequency migration make for a considerably high degree of computational complexity that makes analysis all the more difficult.

In this paper, we report on our analysis of SAR by computer simulation to assess electromagnetic wave exposure on the human body by a FPU operating in single-input, single-output (SISO) mode. Taking frequency migration in mobile-relay FPUs into account, we obtained analysis results for each of the 700-MHz, 1.2-GHz, and 2.3-GHz bands for comparison purposes. For this analysis, we used a numerical human-body model having the average body shape of an adult Japanese male, and assuming an environment in which an announcer and driver riding a broadcast van are positioned near transmitting antennas mounted on the van's roof, we adjusted the posture of this model for each of these subjects. Furthermore, considering that this analysis would be difficult to perform on a standard workshop given the high computational complexity of SAR simulations especially in the 1.2-GHz and 2.3-GHz bands, we performed the analyses using the TSUBAME2.0 supercomputer.

2 Computational Model

2.1 Antenna Model

The structures of the two-stage collinear antennas used in the study of this paper and photos of these antennas are shown in Figs. 1 and 2, respectively. Specifically, the antenna for evaluation in the 700-MHz band was the two-stage collinear antenna currently used by NHK for remote broadcasting of marathons and long-distance relay races [9]. This type of antenna structure is generally used for transmitting signals in mobile relays. In addition, the antennas for evaluation in the 1.2-GHz and 2.3-GHz bands were two-stage collinear antennas that we designed and constructed as prototypes giving them an antenna gain and radiation pattern nearly the same as that of the 700-MHz band for comparison purposes [10].

The radiation patterns of the transmitting antennas of Figs. 1 and 2 are shown in Figs. 3 – 5. The frequencies targeted for analysis in this study were 800 MHz in the 700-MHz band, 1.27 GHz in the 1.2-GHz band, and 2.35 GHz in the 2.3-GHz band.

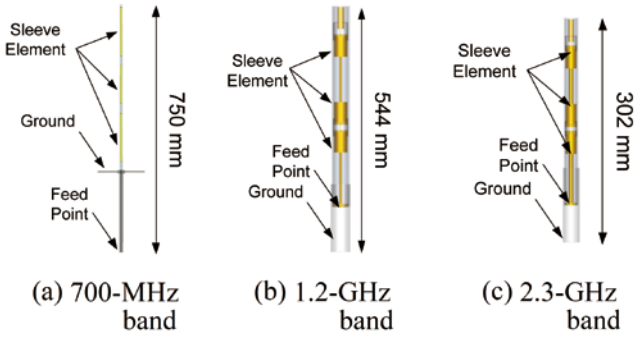

Fig. 1 Antenna structures

Fig. 2 Prototype transmitting antennas (from the left: 700-MHz band, 1.2-GHz band, 2.3-GHz band)

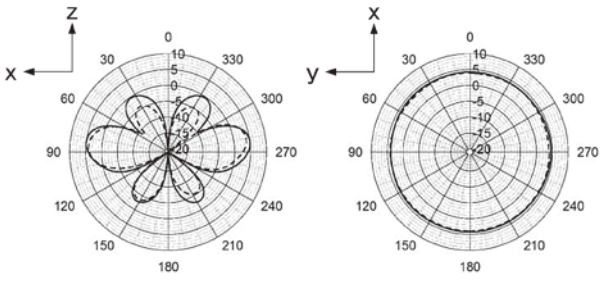

Fig. 3 Radiation pattern (700-MHz band: 800 MHz)

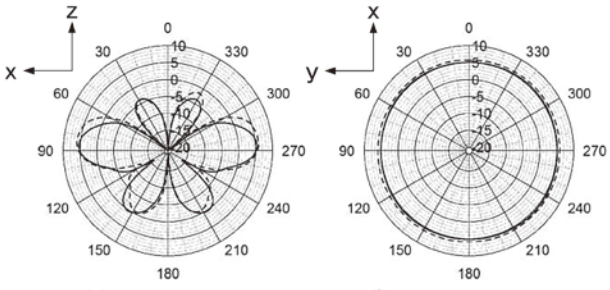

Fig. 4 Radiation pattern (1.2-GHz band: 1.27 GHz)

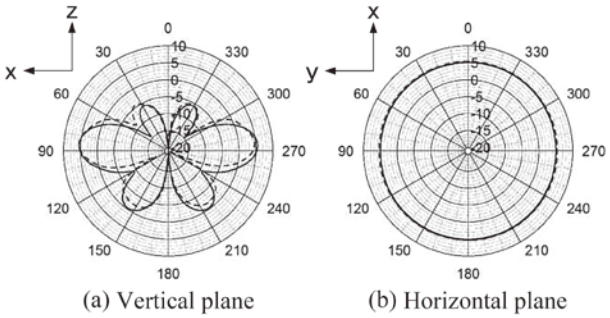

Fig. 5 Radiation pattern (2.3-GHz band: 2.35 GHz)

In Figs. 3 – 5, the amplitude values represent antenna gain [dBi] and the solid and broken lines the computed and measured values, respectively. It can be seen that the computational model and measured values are nearly in agreement, which indicates that we were able to perform an analysis with sufficient accuracy. It can also be seen from these figures that the antennas for these three frequency bands have nearly the same radiation pattern.

2. 2 Numerical Human-body Model

The numerical human-body model used in this study is shown in Fig. 6. Specifically, we used an adult Japanese male model described in Ref. [11] and deformed this model to fit the postures of the announcer and driver at the time of mobile FPU operation using free form deformation (FFD) [12]. This model consists of 51 types of body tissues and has a spatial resolution of 2 mm.

In our analysis, we set individual electrical constants for all of the body tissues in this numerical human-body model. We used the resource described in Ref. [13] to obtain the values of these electrical constants at various frequencies.

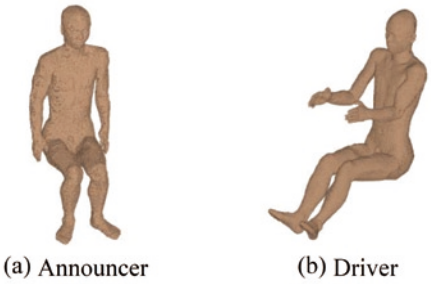

Fig. 6 Numerical human-body model used in this study

2. 3 Analysis Model

Our aim was to analyze the announcer's and driver's state of exposure to electromagnetic waves emitted from transmitting antennas mounted on the broadcast van under actual operating conditions. To this end, we created a detailed model of NHK's RS-2 broadcast van (5980 × 2300 × 3300 mm) starting with a CAD model of the vehicle and used the numerical human-body model shown in Fig. 6 for the announcer and driver. Furthermore, to assess the effects of the vehicle shape shown in Figs. 7 and 8, we also analyzed the models shown in Figs. 9 and 10 with the vehicle deleted. Here, the positional relationships between the antennas and the numerical human-body model in Figs. 9 and 10 are the same as those of Figs. 7 and 8 with just the shape of the vehicle removed.

In Figs. 7 and 9, the announcer is sitting in the announcer's booth at the rear of the broadcast van and the height of the antennas are nearly the same as that of the announcer's body. Figures 8 and 10 show the model of the driver sitting in the driver's seat of the broadcast van.

There are two types of transmitting antennas mounted on the broadcast van: one for transmitting signals to a terrestrial base station and the other mounted 1.87m behind the former for transmitting signals to a helicopter. The mounting positions of these antennas are those currently used by NHK in mobile relays of marathons and long-distance relay races [11]. We performed the analysis under the condition that both antennas are transmitting continuously with the same transmission power. The antennas shown in Fig. 1 were used for either type of antenna depending on the transmission frequency. In addition, the distances between the human body (announcer) and the base-station-directed transmitting antenna and helicopter-directed transmitting antenna in Figs. 7 and 9 were approximately 3.3 m and 1.4 m, respectively, and the distances between the human body (driver) and the base-station-directed transmitting antenna and helicopter-directed

transmitting antenna in Figs. 8 and 10 were approximately 1.3 m and 2.5 m, respectively.

The heights of the base-station-directed and helicopter-directed transmitting antennas were both set to 3.8 m above the ground to comply with Japan's Road Traffic Act that stipulates that the height of such a transmitting antenna be no greater than 3.8 m from ground level.

We performed an electromagnetic field analysis for both the base-station-directed transmitting antenna and helicopter-directed transmitting antenna for each the three frequency bands described earlier under the conditions shown in Figs. 7 – 10. We used CST Microwave Studio (CST MWS) [14] for conducting the electromagnetic field analysis and SAR calculations.

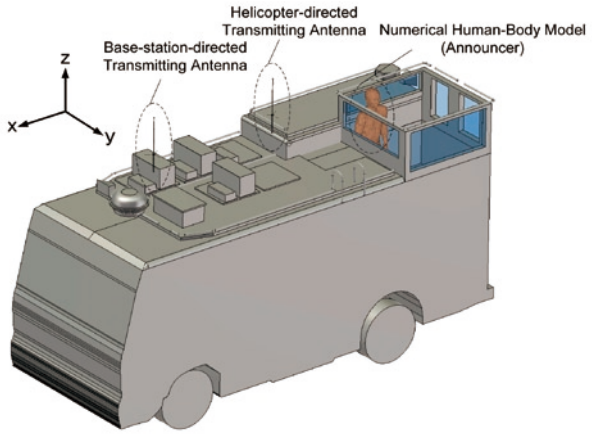

Fig. 7 Analysis model (condition A)

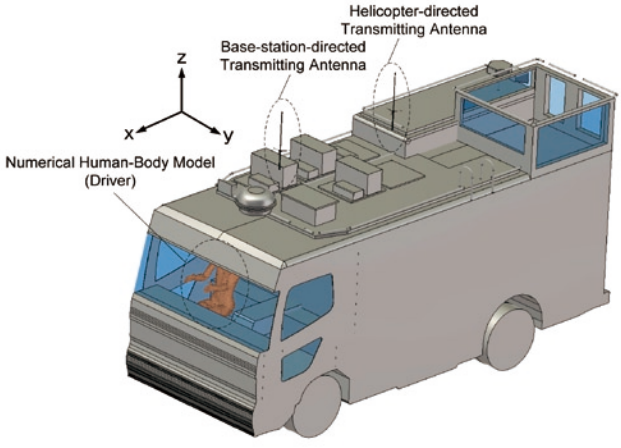

Fig. 8 Analysis model (condition B)

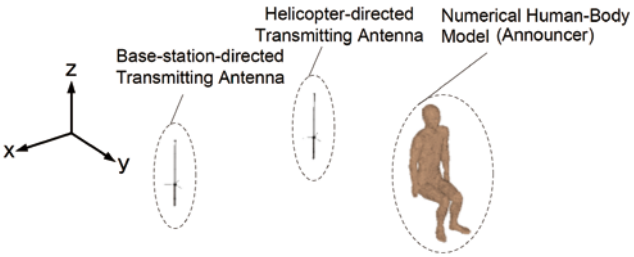

Fig. 9 Analysis model with no broadcast van (condition C)

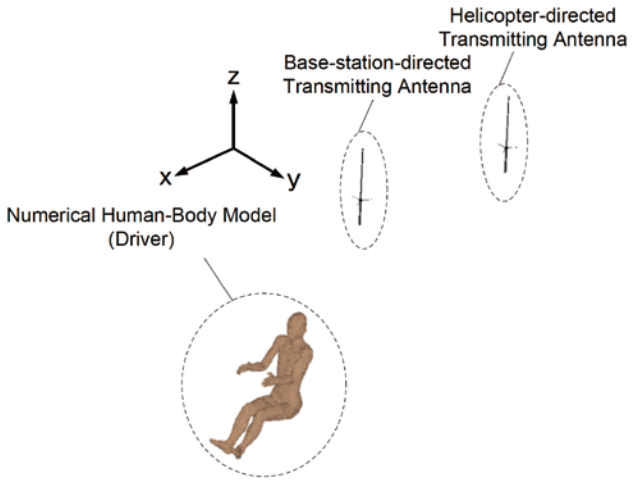

Fig. 10 Analysis model with no broadcast van (condition D)

3 SAR Analysis

3.1 SAR Computational Method

In keeping with the international use of Eq. (1) for calculating SAR [15], we likewise based our calculations on this equation.

$$\mathrm{SAR} = \frac{\sigma}{\rho} E^2 \quad [\mathrm{W/kg}] \qquad (1)$$

Here, σ is conductivity of human-body tissue [S/m], ρ is density of the tissue [kg/m^3], and E is the effective value of electric field strength [V/m]. In this SAR evaluation, we evaluated 10g average local SAR [6] obtained by averaging SAR across any 10 grams of human-body tissue and whole-body average SAR. Furthermore, we targeted a general environment within radio-radiation protection guidelines. In this type of environment, 10g average local SAR must not exceed 2 [W/kg] while whole-body average SAR must not exceed 0.08 [W/kg].

3.2 SAR Analysis of Transmission from the Base-station-directed Transmitting Antenna

We analyzed SAR for the case of transmission from the base-station-directed transmitting antenna under each of the conditions of Figs. 7 – 10 and for operation in the 700-MHz, 1.2-GHz, and 2.3-GHz frequency bands. The maximum values obtained for 10g average local SAR for each condition are listed in Table 1 and those for whole-body average SAR are listed in Table 2. The maximum transmission power that could be used was 5W, 25W, and 40W for the 700-MHz, 1.2-GHz, and 2.3-GHz bands, respectively.

First, in Table 1, on comparing SAR across these frequency bands, it can be seen that SAR becomes larger along with the increase in transmission power in the 1.2-GHz and 2.3-GHz bands. We can also compare SAR results here across conditions A – D with respect to body-antenna positional relationship and vehicle presence/absence. To begin with, it can be seen that the presence/absence of the broadcast van (conditions A and C) results in no major difference in announcer SAR regardless of the frequency band. We attribute this to the fact that the announcer is situated in an essentially open environment despite the presence of a window frame so that there is practically no change in SAR. In contrast, on comparing driver SAR between conditions B and D, it can be seen that SAR with the vehicle present is as much as 1/100 smaller that that with no vehicle present. We attribute this result to the fact that the vehicle provides the driver with considerable shielding compared to that provided to the announcer.

Next, SAR results for whole-body average SAR in Table 2 follow the same trend as those for 10g average local SAR. It can be seen that vehicle shielding has a large effect on driver SAR.

The results in Table 1 and 2 show that maximum values for 10g average local SAR and whole-body average SAR did not exceed 0.04 [W/kg] and 0.001 [W/kg], respectively.

Table 1 Maximum values for 10g average local SAR [W/kg] (base-station-directed)

Analysis model	800 MHz	1.27 GHz	2.35 GHz
Condition A	0.0032	0.018	0.038
Condition B	0.000014	0.00048	0.00049
Condition C	0.0028	0.012	0.03
Condition D	0.0035	0.029	0.042

Table 2 Maximum values for whole-body average SAR [W/kg] (base-station-directed)

Analysis model	800 MHz	1.27 GHz	2.35 GHz
Condition A	0.00014	0.00077	0.00075
Condition B	0.0000016	0.000021	0.000017
Condition C	0.00011	0.00052	0.00043
Condition D	0.00011	0.00074	0.0011

3. 3 SAR Analysis of Transmission from the helicopter-directed Transmitting Antenna

We also analyzed SAR for the case of transmission from the helicopter-directed transmitting antenna under each of the conditions of Figs. 7 – 10 and for operation in the 700-MHz, 1.2-GHz, and 2.3-GHz frequency bands. The maximum values obtained for 10g average local SAR for each condition are listed in Table 3 and those for whole-body average SAR are listed in Table 4. The maximum transmission power that could be used was 5W, 25W, and 40W for the 700-MHz, 1.2-GHz, and 2.3-GHz bands, respectively, as in the case of the base-station-directed transmitting antenna.

Table 3 Maximum values for 10g average local SAR [W/kg] (helicopter-directed)

Analysis model	800 MHz	1.27 GHz	2.35 GHz
Condition A	0.0071	0.034	0.023
Condition B	0.00013	0.0001	0.000025
Condition C	0.0087	0.029	0.036
Condition D	0.00021	0.0041	0.0033

Table 4 Maximum values for whole-body average SAR [W/kg] (helicopter-directed)

Analysis model	800 MHz	1.27 GHz	2.35 GHz
Condition A	0.00021	0.0012	0.0011
Condition B	0.0000012	0.0000033	0.000001
Condition C	0.00018	0.0011	0.00093
Condition D	0.000013	0.0003	0.0002

Examining Table 3, we can see that the results for announcer SAR under conditions A and C are larger all around than the results of Table 1 since the helicopter-directed transmitting antenna is closer to the announcer than the base-station-directed transmitting antenna. On the other hand, values of 10g average local SAR under conditions B and D are smaller since the helicopter-directed transmitting antenna is further away from the driver. In addition, the presence/absence of the broadcast van has the same effect on driver SAR as in Table 1 showing that the effect of vehicle shielding is large. The results in Table 4 for whole-body average SAR follow the same trend as that in Table 3.

The results in Table 3 and 4 show that maximum values for 10g average local SAR and whole-body average SAR did not exceed 0.04 [W/kg] and 0.001 [W/kg], respectively.

3. 4 Discussion

Current FPU operation in the 700-MHz band consists of ongoing, simultaneous transmission from the base-station-directed transmitting antenna and helicopter-directe transmitting antenna. There is therefore a need to evaluate 10g average local SAR and whole-body average SAR on the basis of a total SAR value that combines the individual values from each of the above transmitting antennas assuming the same operation format.

Total values for 10g average local SAR from Tables 1 and 3 for conditions A and B are listed in Table 5 and total values for whole-body average SAR from Tables 2 and 4 for conditions A and B are listed in Table 6.

Table 5 Total 10g average local SAR [W/kg]

Analysis model	800 MHz	1.27 GHz	2.35 GHz
Condition A	0.01	0.052	0.06
Condition B	0.00014	0.00058	0.038

Table 6 Total whole-body average SAR [W/kg]

Analysis model	800 MHz	1.27 GHz	2.35 GHz
Condition A	0.00035	0.002	0.0018
Condition B	0.0000028	0.000024	0.00075

The results of Tables 5 and 6 show that total values for the announcer are about 100 times larger than that of the driver for either 10g average local SAR or whole-body average SAR.

They also show, however, that those values are much smaller than the guideline values for a general environment stipulated by radio-radiation protection guidelines for either type of SAR.

We point out here that, while this study did not target any engineering or control personnel riding in the broadcast van, windows (openings) in space occupied by such personnel are smaller than the vehicle's front windshield, which suggests that these personnel would have SAR values that are much smaller than that of the driver and therefore less than the guideline values stipulated by radio-radiation protection values.

Conclusion 4

Taking into account government plans for frequency migration of FPUs used for mobile relays, we investigated electromagnetic wave exposure on human bodies positioned close to transmitting antennas installed on the roof of a broadcast van under SISO operation.

Assuming antenna position and operation the same as that of the currently used 700-MHz band, the results of our study revealed that 10g average local SAR and whole-body average SAR take on large values due to high transmission power at 25W for the 1.2-GHz band and 40W for the 2.3-GHz band and large conductivity of human-body tissue in these bands compared to the 700-MHz band. Nevertheless, it was found that the SAR values obtained were much smaller than the guideline values for a general environment as stipulated by radio-radiation protection guidelines.

In future research, we plan to study differences in SAR according to antenna installation position and MIMO operation and to investigate techniques for reducing SAR.

Acknowledgement

The numerical calculations on this article were carried out on the TSUBAME2.0 supercomputer in the Tokyo Institute of Technology. We express our gratitude to having the opportunity to use the TSUBAME2.0 supported by the MEXT Open Advanced Research Facilities Initiative.

References

[1] "Portable OFDM Digital Transmission System for Television Program Contribution," ARIB STD-B33, ver. 1.1, Nov. 2005.

[2] "Action Plan for Spectrum Reallocation," Ministry of Internal Affairs and Communications, revised Sep. 2012, http://www.tele.soumu.go.jp/e/adm/freq/search/actionplan/index.htm

[3] T. Nakagawa, T. Ikeda, "Performance Improvement of 2x2 STTC-MIMO-OFDM System," ITE Technical Report, vol.36, no.10, BCT2012-48, pp.69-72, Feb. 2012.

[4] "Safety Guide Line for use of Radio Waves," Ministry of Internal Affairs and Communications, 1997.

[5] "Method of measuring specific absorption rate for the radio equipment to be used near the human body excluding the human head," Ministry of Internal Affairs and Communications, Oct. 2011.

[6] "IEEE recommended practice for measurements and computations of radio frequency electromagnetic fields with respect to human exposure to such fields, 100 kHz-300 GHz," IEEE Standard C95.3-2002, 2003.

[7] S. Akimoto, S. Kikuchi, K. Saito, M. Takahashi, K. Ito, "Calculations of SAR in Abdomen Using Numerical Human Model by Normal Mode Helical Antenna at 150MHz," IEICE Trans. Comm., vol.J92-B, no.1, pp.304-311, Jan. 2009.

[8] N. Kogo, T. Ikeda, "Effect of Human Posture on Antenna Performance of Transceiver for Push-to-Talk Communication Line in VHF and UHF Bands," PIERS2012, p.468, Aug. 2012.

[9] N. Kogo, T. Ikeda, "Analysis of SAR due to FPU in 700MHz Band considering its Operation," ITE Technical Report, vol.36, no.37, BCT2012-83, pp.25-28, Sep. 2012.

[10] N. Kogo, M. Yatagai, F. Murakami, T. Ikeda, "Propagation Characteristics of FPU for Road Race in Lake Biwa Mainichi Marathon," ITE Technical Report, vol.36, no.30, BCT2012-70, pp.41-44, Jul. 2012.

[11] "The Development of Whole-Body High-Resolution Voxel Models of the Average Japanese Adult Male and Female," Trans. of Japanese Society for Medical and Biological Engineering, vol.40, no.4, pp.45-52, Dec. 2002.

[12] T. Nagaoka, S. Watanabe, "Postured voxel-based human models for electromagnetic dosimetry," Phys. Med. Biol., 53(24), pp.7047-7061, Dec. 2008.

[13] http://transition.fcc.gov/oet/rfsafety/dielectric.html

[14] T. Weiland, "RF & Microwave Simulators - From Component to System Design" Proceedings of the European Microwave Week (EUMW 2003), vol.2, pp. 591-596, Oct. 2003.

[15] "Safety levels with respect to human exposure to radio frequency electromagnetic fields, 3kHz to 300GHz," ANSI/IEEE Standard C95.1-2005, October 2005.

All-Atom Simulation of a Cell Membrane System of Photosynthetic Bacteria Using Large-Scale GPU Calculation

Masakazu Sekijima*, Takuro Udagawa****

* Global Scientific Information and Computing Center, Tokyo Institute of Technology
** Graduate School of Information Science and Engineering, Tokyo Institute of Technology

In purple photosynthetic bacteria, photosynthesis takes places in vesicles of the cell membrane, and these vesicles are known as chromatophores. There are few membrane protein types in the chromatophores. These include proteins such as LH1 antenna complexes (LH1) and LH2 antenna complexes (LH2), which harvest light, as well as photoreaction centers (RC) and bc1 complexes. In recent years, it has become clear that the vesicle form in chromatophore membranes is determined by active self-organization via LH1 and LH2.In this study, to understand the mechanism of chromatophore self-organization at the atomic level and the determination of membrane form, a full simulation program was conducted. The simulation was accomplished using TSUBAME 2.0 with 700 nodes, each with 2 CPUs and 3 GPUSs, on a model constructed from information obtained from an atomic force microscope.

Introduction 1

When plants receive sunlight, water (through the roots), and carbon dioxide (from air), they synthesize carbohydrates and oxygen. This phenomenon is known as photosynthesis; it is a process where light energy is converted into chemical energy. Based on the fact that the solar constant is 1366 W/m2, the energy that the Earth receives from the Sun can be derived as 174 PW. 47% of this energy reaches the surface of the Earth. Research and development on the construction of an energy network that can store solar energy as chemical energy, which can then be retrieved when needed, is currently being carried out [1,2].

Photosynthetic bacteria are generally found in anaerobic water areas, such as lakes and marshes. They synthesize ATP (Adenosine Triphosphate) by anoxygenic photosynthesis, using a homogenous photochemical system. These photosynthetic bacteria offer a high degree of freedom in terms of gene recombination and are important in basic research for clarifying topics such as the basic principles of energy conversion mechanisms, the smallest units of photosynthesis, and the evolution of photosynthetic organs.

In the light-harvesting system of purple photosynthetic bacteria, shown in Figure 1, photosynthesis occurs in the vesicles of cell membranes; these vesicles are known as chromatophores. The types of membrane proteins are few, and include, for example, LH1 antenna complexes (light harvesting complex 1) and LH2 antenna complexes (light harvesting complex 2), which harvest light, as well as photoreaction centers (RC) and cytochrome bc1 complexes. Species that contain no LH2, such as Rhodospirillum (Rsp.) rubrum, also exist; however, even in these species, LH1 exists in the purple photosynthetic bacteria [3].

Experiments in recent years have shown that the form of the vesicles in the chromatophore membranes is determined by active selforganization by LH1 and LH2. Thus, gaining knowledge on how membrane form changes according to the self-organization of these membrane proteins can also lead to a better understanding of the photosynthesis mechanism.

In this study, to understand, the mechanism of selforganization and the determination of membrane form at the atomic level, molecular dynamics simulation was conducted on a model [5,6] constructed from an image obtained from an atomic force microscope. This model is a large system involving approximately 20 million atoms when all proteins, lipid membranes, and surrounding water molecules are united.

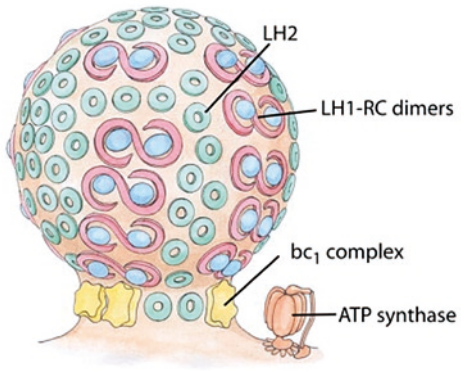

Fig. 1 Diagram[4] focusing on the light-harvesting complexes and reaction in purple photosynthetic bacteria.

**Current position: Japan Atomic Energy Agency

Molecular dynamics 2

Molecular Dynamics: MD is a simulation method where the behavior of molecules is determined using classical mechanics. For each atom comprising the system, interaction forces between surrounding atoms are calculated for miniscule time increments; and the time evolution of threads is sought by solving Newton's equation of motion, ma = F, using numerical integration. Molecular dynamics that targets biomolecules is often used for molecular dynamics analysis, structural optimization, and protein binding site prediction [7]. In molecular dynamics, the interaction of atoms is calculated using force fields.

$$U(\mathbf{q}) = \sum_{bonds} k^b (b - b_0)^2 + \sum_{angles} k^\theta (\theta - \theta_0)^2 + \sum_{torsions} V_n \left[1 + \cos^2(n\phi - \phi_0)\right] + \sum_{i,j \in atoms} \varepsilon_{ij} \left[\left(\frac{r_{ij}^0}{r_{ij}} \right)^{12} - 2 \left(\frac{r_{ij}^0}{r_{ij}} \right)^6 \right] + \sum_{i,j \in atoms} \frac{q_i q_j}{r_{ij}} \quad (1)$$

Equation (1) is a widely used force field called AMBER [8]. The first term represents the length of the chemical bond, the second term the angle of the chemical bond, the third term the dihedral angle, the fourth term the van der Waals force, and the fifth term the electrostatic interaction force. Of these forces, the van der Waals force and electrostatic interaction force are not based in chemical bonds. They are forces that also work between distant atoms; therefore, the computational complexity increases by a power of twice the number of atoms. In many instances, at least 90 % of the execution time of molecular dynamics simulation is spent on the evaluation of these two types of forces.

After first calculating the interaction forces, the equation of motion is used to calculate atom coordinates and velocities in the next step of the simulation. Time widths used in molecular dynamics simulations are normally very small time frames of around 1–2 femtoseconds. Calculations in the order of nanoseconds or microseconds are required in order to obtain a scientifically significant result. Thus, it is necessary to conduct the simulation with more than a few million steps. Therefore, molecular dynamics has a high calculation cost, making it a type of computation where improvements in speed are strongly demanded.

NAMD 3

NAMD [9] is free-of-charge molecular dynamics simulation program developed by the Theoretical and Computational Biophysics Group of the University of Illinois. It is written using Charm++ [10], developed at the Parallel Programming Laboratory (also of the University of Illinois) and is designed as a high performance simulator of macromolecular systems.

An innovation in NAMD for improving scalability is the partitioning of interaction force calculations and simulation space. At the start of the simulation, the simulation space is subdivided into units called "patches," which are distributed to each calculation-conducting processor. Each processor handles the data of the coordinates and velocities of atoms included in their respective distributed patches. The sizes of the patches consider account cutoff distance and are set up such that a direct computation section is created for the van der Waals forces and electrostatic interaction forces. In this way, by accounting for spatial locality, computational complexity and communication between processes can be reduced even for large-scale systems.

In the calculation of interaction forces, computing objects are defined by force-type. In "compute object," where forces from chemical bonds are calculated, the process through which the force is calculated is chosen based on which patch the atom requiring computation belongs to. Using this process, calculations of atoms that straddle multiple patches and processes can be done efficiently, and the reduction of data traffic is possible.

The calculation of van der Waals forces and electrostatic interaction forces, both of which are independent of chemical bonds, takes up 80% –90% of the execution time in the molecular dynamics method. In NAMD, a GPU is apportioned for these calculations to make them faster. In the NAMD package, multiple CPU processes share a single GPU and the calculation is done on non-bonding forces for the atoms in the space belonging to that process. In this way, by applying the GPU only to non-bonding force calculations, and by having the GPU shared in multiple CPU processes, an implementation is conducted that is flexible and has high scalability with respect to the computer.

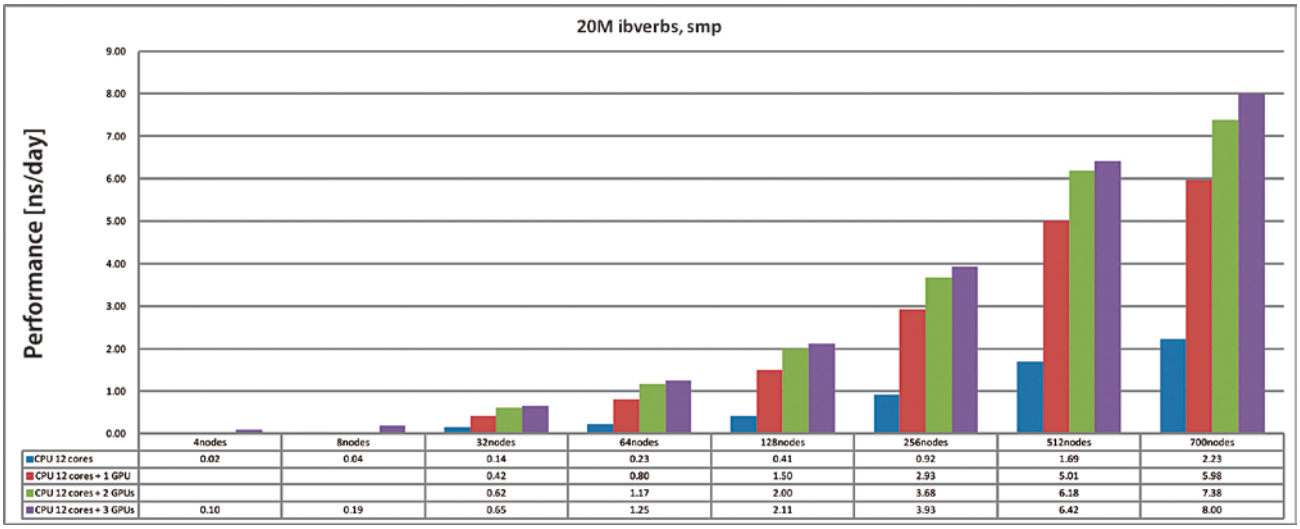

	4nodes	8nodes	32nodes	64nodes	128nodes	256nodes	512nodes	700nodes
CPU 12 cores	0.02	0.04	0.14	0.23	0.41	0.92	1.69	2.23
CPU 12 cores + 1 GPU			0.42	0.80	1.50	2.93	5.01	5.98
CPU 12 cores + 2 GPUs			0.62	1.17	2.00	3.68	6.18	7.38
CPU 12 cores + 3 GPUs	0.10	0.19	0.65	1.25	2.11	3.93	6.42	8.00

Fig. 2 NAMD performance benchmark

Performance measurement using a GPGPU for a large-scale molecular dynamics simulation 4

In this study, we used a 700 node, 2100 GPU in TSUBAME 2.0, and measured the performance benchmark data for NAMD. The purple photosynthetic bacteria system used was an extremely large system with a total of 20,305,122 atoms, consisting of proteins, lipid bilayers, and solvent. The versions of the NAMD and Charm++ used were 2.8 and 6.3.2, respectively. For compiling, gcc version 4.3.4 and cuda toolkit 4.0 were used. In the measurement, the number of nodes was increased from 4 to 700, and the strong scaling performance of the NAMD in response to the increase in nodes was examined. In addition, data was collected in relation to using 0-3 nodes per GPU.

In Figure 2, the result is displayed in ns/day. In other words, it is displayed in terms of the number of seconds the simulation progresses in one day. Normally, when the number of nodes and GPUs increases, performance often does not improve because the data transfer and synchronization cost increase along with the increase of computational complexity. However, when using NAMD, when increasing both the number of nodes and GPUs, we were able to obtain performance improvement up until 700 nodes and 2100 GPU. Not only scaling performance but also the performance improvement caused by use of GPU is noteworthy. When using NAMD, 1 GPU improved performance by an approximate factor of three, compared to only using CPUs.

Analysis of self-organization of light-harvesting proteins using a large-scale molecular dynamics simulation 5

In our study, a molecular dynamics simulation was conducted on a purple photosynthetic bacterium molecular model created by Klaus Schulten's research group at the University of Illinois. We used 700 nodes and 2100 GPU in TSUBAME 2.0. Data input/output was costly, and although the performance dropped under the benchmark, we succeeded in executing a simulation of 7 nanoseconds in total during the grand challenge period.

In Figure 3, we show changes in the system's potential energy over 7 nanoseconds. Potential energy greatly fluctuates when the system is unstable or when the simulation is not running successfully. In this result, the potential energy is mostly maintained at a set value, and so it can be determined that we were able to conduct a stable simulation.

Next, we analyzed the self-organization process of light-harvesting proteins. It has been reported that in the photosynthetic reaction process of purple photosynthetic bacteria, self-organization of light-harvesting proteins occurs in relation to the reaction center (RC). In this study, we decided to focus on, and conduct an analysis on, changes of the center-of-gravity distances between LH1 complexes, with reaction centers, and LH2 complexes, without reaction centers. As we show in Figure 4, each LH1 complex and LH2 complex was distinguished by being corresponded with a character of the alphabet. A-Z and a-j were assigned to the LH2 complexes, while k-q were assigned to the LH2 complexes.

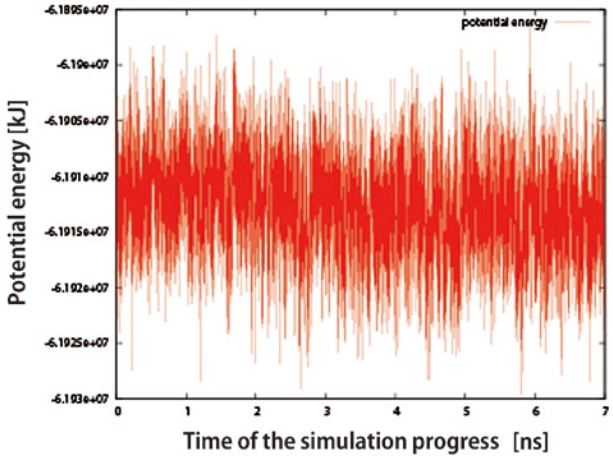

Fig. 3 Temporal change in potential energy

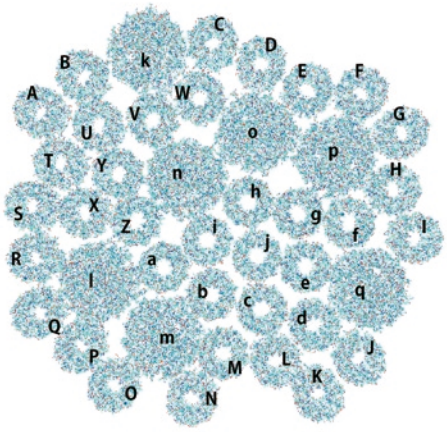

Fig. 4 Labels for each protein

In the chart shown in Figure 5, the distance from each LH1 complex to nearby LH2 complexes is plotted over time. Tendencies can be observed from looking at this chart; for example, as time passed the center-of-gravity distance gradually shortened between LH1 complex l and LH2 complex a and Q, LH1 complex p and LH2 complex H, and LH1 complex n and LH2 complex V. In particular, whereas the distance between LH1 complex n and LH2 complex V is shortening, the distance between LH1 complex k and LH2 complex V is mostly constant; and due to the fact that the distance between LH1 complex n and LH2 complex i shows an increasing tendency, it can be inferred that LH1 complex n is being drawn in toward LH2 complex V.

Conclusion 6

The purpose of this study was to analyze protein interaction in the chromatophores of purple photosynthetic bacteria, and to evaluate the performance of a GPGPU. This was done by conducting a molecular dynamics simulation, using TSUBAME 2.0 with 700 nodes, on a large-scale molecular model of the light-harvesting complexes and reaction centers of purple photosynthetic bacteria.

Molecular dynamics simulations are occasionally executed over a period of a few months; when the system becomes larger, a longer execution time is required. Because a GPU is installable and is
relatively cheap, and is considered to improve on computation speed, there is much hope being placed on it as an option for researchers to use in order to shorten the time required for molecular dynamics simulations. In this study, even in a 20,305,122-atom system used for performance evaluation, when using GPU, compared to simulation using only CPU, it was possible to execute at up to 5.1 times the speed with 128 nodes, and approximately 3.6 times the speed with 700 nodes. Furthermore, as we have shown separately, energy consumption can also be limited by using the GPU [11].

The phenomenon of multiple proteins interacting in a membrane environment is difficult to measure when using conventional small-molecular-system simulations. It is a phenomenon that can only be observed by a large-scale system and a computing environment that is capable of executing the simulation. In this study, we used the large-scale computing environment of TSUBAME 2.0, accelerated by a GPU, to conduct a 7- nanosecond simulation in a period of approximately three days. We succeeded in simulating the process of protein self-organization in purple Although we were able to observe trends in the early stages of the self-organization process from the results of this study, we could not reach a full recreation of the phenomenon. In the future, further execution of simulations and additional analyses will be needed. photosynthetic bacteria. However, as the molecular system size increases, the simulation time lengthens.

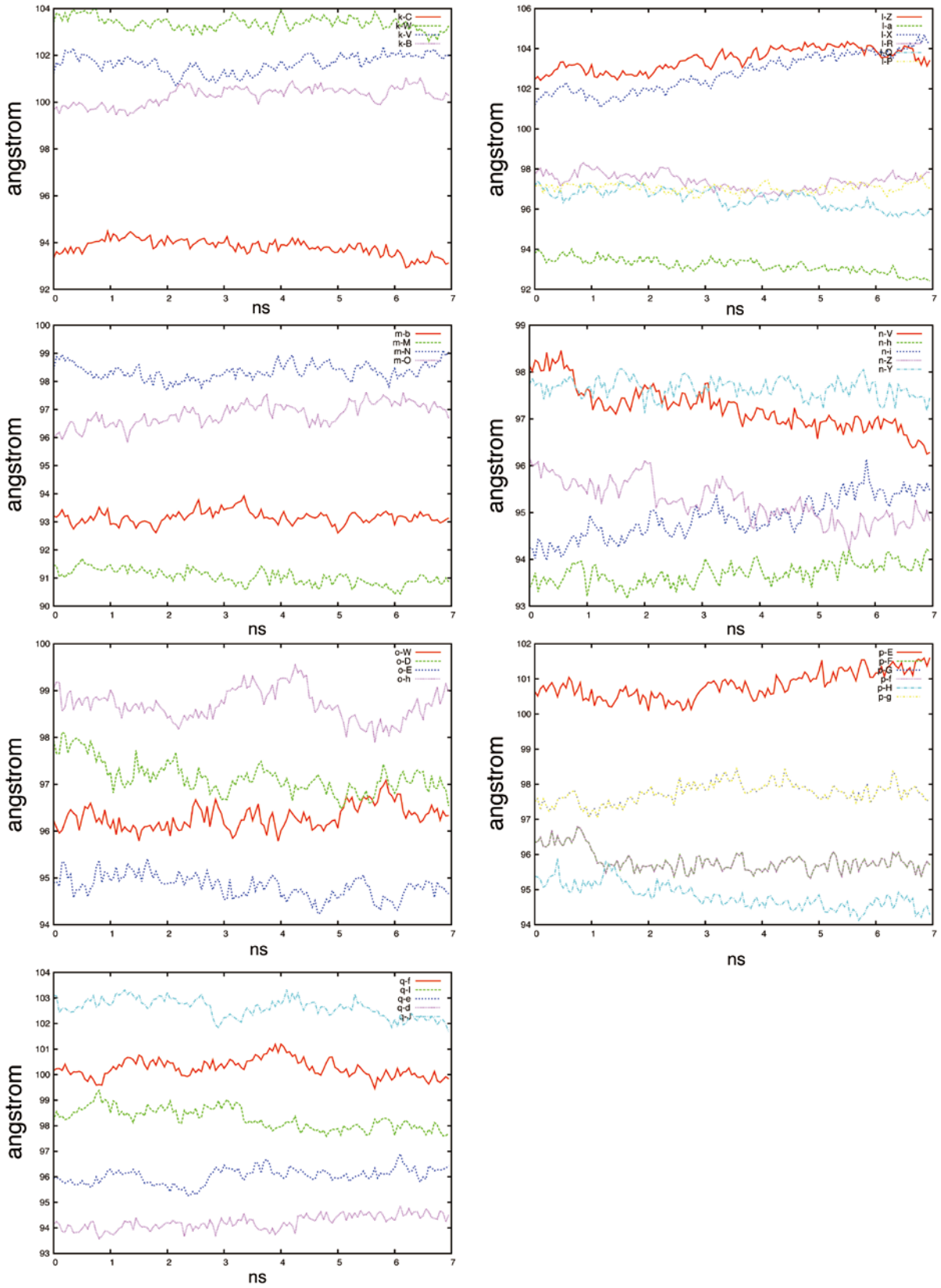

Fig. 5 Changes in distance between each LH1 and nearby LH2s.

All-Atom Simulation of a Cell Membrane System of Photosynthetic Bacteria Using Large-Scale GPU Calculation

Acknowledgements

These computations were executed as the TSUBAME Grand Challenge Program, Category B in 2011 fall and we express our special thanks to having a chance to use the TSUBAME resources and the GSIC staffs who supported our project. We acknowledge Professor K. Schulten and Dr. Jim Philips for technical support of NAMD and structure of chromatophores.

References

[1] A. Listorti, J. Durrant and J. Barber, Artificial photosynthesis: Solar to fuel, Nature Materials 8, pp. 929 - 930 (2009).

[2] M. W. Kanan and D. G. Nocera, In Situ Formation of an Oxygen-Evolving Catalyst in Neutral Water Containing Phosphate and Co2+, Science 321, pp. 1072-1075 (2008).

[3] W. Kühlbrandt, Chlorophylls galore, Nature 411, pp. 896-899 (2001).

[4] D.E. Chandler, J. Hsin, C. B. Harrison, J. Gumbart, K. Schulten 95, pp.2822-2836 (2008).

[5] M. K. Sener, J. Hsin, L. G. Trabuco, E. Villa, P. Qian, C. N. Hunter, and K. Schulten, Structural model and excitonic properties of the dimeric RC-LH1-PufX complex from Rhodobacter sphaeroides, Chemical Physics 357, pp.188-197, (2009).

[6] J. Hsin, J. Strümpfer, M. Sener, P. Qian, C. N. Hunter, and K. Schulten. Energy transfer dynamics in an RC-LH1-PufX tubular photosynthetic membrane, New Journal of Physics 12 , pp. (2010).

[7] M. Sekijima, C. Motono, S. Yamasaki, K. Kaneko, and Y. Akiyama, Molecular dynamics simulation of dimeric and monomeric forms of human prion protein: Insight into dynamics and properties, Biophysical Journal 85, pp.1176-1185 (2003).

[8] [J.W. Ponder and D.A. Case, Force fields for protein simulations, Advances in Protein Chemistry 66, pp.27-85 (2003).

[9] J. C. Phillips, R. Braun, W. Wang, J. Gumbart, E. Tajkhorshid, E. Villa, C. Chipot, R. D. Skeel, L. Kale, and K. Schulten, Scalable molecular dynamics with NAMD, Journal of Computational Chemistry 26, pp.1781-1802 (2005).

[10] L. V. Kale, E. Bohm, C. L. Mendes, T. Wilmarth and G. Zheng, Programming Petascale Applications with Charm++ and AMPI. In Petascale Computing, Algorithms and Applications, pp. 421-441, Chapman & Hall / CRC Press, ed D Bader (2004).

[11] S. Du, T. Udagawa, T. Endo and M. Sekijima, Molecular Dynamics Simulation of a Biomolecule with High Speed, Low Power and Accuracy Using GPU-Accelerated TSUBAME2.0 Supercomputer, Proceedings of the Asia-Pacific Signal and Information Processing Association Annual Summit and Conference 2011 (APSIPA ASC 2011), pp.1-5, 2011M. Sussman, P. Smereka and S. Osher: A Level Set Approach for Computing Solutions to Incompressible Two-Phase Flow, J. Comp. Phys., Vol. 114, pp.146-159 (1994)

● **TSUBAME e-Science Journal vol.9**

Published 09/09/2013 by GSIC, Tokyo Institute of Technology © ISSN 2185-6028

Design & Layout: Kick and Punch

Editor: TSUBAME e-Science Journal - Editorial room
Takayuki AOKI, Thirapong PIPATPONGSA,
Toshio WATANABE, Atsushi SASAKI, Eri Nakagawa

Address: 2-12-1-E2-6 O-okayama, Meguro-ku, Tokyo 152-8550

Tel: +81-3-5734-2085 Fax: +81-3-5734-3198

E-mail: tsubame_j@sim.gsic.titech.ac.jp

URL: http://www.gsic.titech.ac.jp/

TSUBAME

International Research Collaboration

The high performance of supercomputer TSUBAME has been extended to the international arena. We promote international research collaborations using TSUBAME between researchers of Tokyo Institute of Technology and overseas research institutions as well as research groups worldwide.

Recent research collaborations using TSUBAME

1. Simulation of Tsunamis Generated by Earthquakes using Parallel Computing Technique
2. Numerical Simulation of Energy Conversion with MHD Plasma-fluid Flow
3. GPU computing for Computational Fluid Dynamics

Application Guidance

Candidates to initiate research collaborations are expected to conclude MOU (Memorandum of Understanding) with the partner organizations/ departments. Committee reviews the “Agreement for Collaboration” for joint research to ensure that the proposed research meet academic qualifications and contributions to international society. Overseas users must observe rules and regulations on using TSUBAME. User fees are paid by Tokyo Tech’s researcher as part of research collaboration. The results of joint research are expected to be released for academic publication.

Inquiry

Please see the following website for more details.
http://www.gsic.titech.ac.jp/en/InternationalCollaboration

GSIC
Global Scientific Information and Computing Center